Time–frequency analysis of signals using support adaptive Hermite–Gaussian expansions

Yaşar Kemal Alp [a,b,*], Orhan Arıkan [a]

[a] Department of Electrical and Electronics Engineering, Bilkent University, Ankara TR-06800, Turkey
[b] Radar, Electronic Warfare and Intelligence Systems Division, ASELSAN A.Ş, Ankara TR-06370, Turkey

A B S T R A C T

Since Hermite–Gaussian (HG) functions provide an orthonormal basis with the most compact time–frequency supports (TFSs), they are ideally suited for time–frequency component analysis of finite energy signals. For a signal component whose TFS tightly fits into a circular region around the origin, HG function expansion provides optimal representation by using the fewest number of basis functions. However, for signal components whose TFS has a non-circular shape away from the origin, straight forward expansions require excessively large number of HGs resulting to noise fitting. Furthermore, for closely spaced signal components with non-circular TFSs, direct application of HG expansion cannot provide reliable estimates to the individual signal components. To alleviate these problems, by using expectation maximization (EM) iterations, we propose a fully automated pre-processing technique which identifies and transforms TFSs of individual signal components to circular regions centered around the origin so that reliable signal estimates for the signal components can be obtained. The HG expansion order for each signal component is determined by using a robust estimation technique. Then, the estimated components are post-processed to transform their TFSs back to their original positions. The proposed technique can be used to analyze signals with overlapping components as long as the overlapped supports of the components have an area smaller than the effective support of a Gaussian atom which has the smallest time-bandwidth product. It is shown that if the area of the overlap region is larger than this threshold, the components cannot be uniquely identified. Obtained results on the synthetic and real signals demonstrate the effectiveness for the proposed time–frequency analysis technique under severe noise cases.

© 2012 Elsevier Inc. All rights reserved.

1. Introduction

Since Hermite–Gaussian (HG) functions constitute a natural basis for signals with compact time–frequency supports (TFSs), they have found applications in various fields of signal processing. In image processing, Hermite transform has been proposed for capturing local information [1]. Another image processing application is given in [2] for rotation of images. Also, in [3], HG functions are used for reconstruction of video frames. In telecommunications, highly localized pulse shapes both in time and frequency domains can be generated by using linear combinations of the HG functions [4]. As part of biomedical applications, representation of EEG and ECG signals in terms of HGs also have been proposed [5,6]. In [7], HG functions are used for characterization of the origins of vibrations in swallowing accelerometry signals. An electromagnetics application is reported in [8], where the time domain response of a three-dimensional conducting object excited by a compact TFS function is modeled by using HG expansions to obtain a fast extrapolator based on this expansion. Another electromagnetics application reported in [9], where a new method for evaluating distortion in multiple waveform sets in UWB communications has been proposed. Finally, as signal processing applications, HG functions are used for designing high resolution, multi-window time–frequency representation, where different order HGs are employed to realize multiple windows, and non-stationary spectrum estimation [10–13].

Single or multi-component signals with compact TFSs are frequently encountered in radar, sonar, seismic, acoustic, speech and biomedical signal processing applications [14–19]. Decomposition of such a signal into its components is an important application of time–frequency analysis [20]. For signals whose components have generalized time–bandwidth products of around 1, wavelet and chirplet based signal analysis techniques have been developed [21–23].

In this work, we are proposing a new signal analysis technique for signals whose components may have larger time-bandwidth

* Corresponding author at: Department of Electrical and Electronics Engineering, Bilkent University, Ankara TR-06800, Turkey.
  E-mail addresses: ykemal@ee.bilkent.edu.tr (Y.K. Alp), oarikan@ee.bilkent.edu.tr (O. Arıkan).

products. Such signals are commonly employed in electronic warfare, including radar and sonar applications, because of their high resolution properties. Furthermore, biomedical signals including EEG and ECG have complicated time–frequency structures that significantly benefits from the proposed approach. The proposed technique makes use of adaptive HG basis expansion to estimate individual signal components. It is a well-known fact that HG functions form an orthonormal basis for the space of finite energy signals which are piecewise smooth in every finite interval [24]. What makes HGs special among other types of basis functions is their optimal localization properties in both time and frequency domains. For any circular TFS around the origin, HGs provide the highest energy concentration inside that region [25–27]. Therefore, if a signal component has a circular TFS around the origin, its representation by using the HG basis provides the optimal representation for a given number of representation order. However, if the signal component has a non-circular TFS positioned away from the origin, its HG representation is no longer optimal. Here, we propose an adaptive pre-processing stage where TFS of the signal component is transformed to a circular one centered around the origin so that it can be efficiently represented by HGs. The expansion order is estimated by a noise penalized costm function. Then, the desired representation is obtained by back transforming the identified signal component. For signals with multiple components that do not have overlapping TFSs, an EM based iterative procedure is proposed for joint analysis and expansion of individual signal components in HG basis.

The outline of the presentation is as follows. In Section 2, we give a brief review of HG functions and emphasize their fundamental properties. In Section 3, the proposed pre-processing stage is introduced. EM based iterative component estimation for analysis of multi-component signals and determination of optimal expansion orders are explained in Section 4. Results on synthetic and real signals are provided in Section 5. Conclusions are given in Section 6.

Note that, unless otherwise is stated, the integrals are computed in the $(-\infty, \infty)$ interval. Bold characters denote vectors, $(.)^H$ and $(.)^*$ are used for vector Hermitian and complex conjugation operations.

2. Review of Hermite–Gaussian functions

HG functions form a family of solutions to the following nonlinear differential equation:

$$f''(t) + 4\pi^2 \left(\frac{2n+1}{2\pi} - t^2 \right) f(t) = 0. \tag{1}$$

The nth order HG function $h_n(t)$ is related to the nth order Hermite polynomial $H_n(t)$ as

$$h_n(t) = \frac{2^{1/4}}{\sqrt{2^n n!}} H_n(\sqrt{2\pi} t) e^{-\pi t^2}, \tag{2}$$

where, with the initialization of $H_0(t) = 1$ and $H_1(t) = 2t$, $H_n(t)$ can be recursively obtained as

$$H_{n+1}(t) = 2t H_n(t) - 2n H_{n-1}(t). \tag{3}$$

Therefore, HG functions can also be computed recursively. A detailed discussion on HG functions and Hermite polynomials are available in [28] and [29], respectively. HG functions, of which the first four are shown in Fig. 1, form an orthonormal basis for the space of finite energy signals which are piecewise smooth in every finite $[-\tau, \tau]$ interval [24]. Hence, if $s(t)$ is in this space, it can be represented as
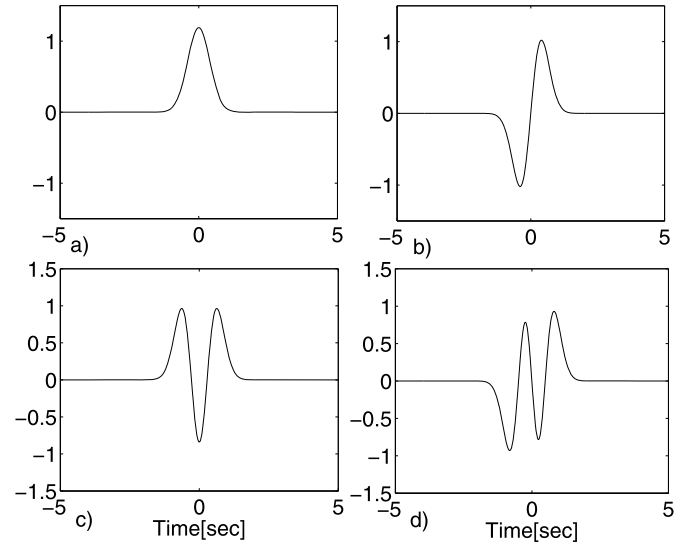

Fig. 1. The first four HG functions: (a) $h_0(t)$; (b) $h_1(t)$; (c) $h_2(t)$; (d) $h_3(t)$.

$$s(t) = \sum_{n=0}^{\infty} \alpha_n h_n(t), \tag{4}$$

where the expansion coefficients are

$$\alpha_n = \int h_n(t) s(t) \, dt. \tag{5}$$

Furthermore, HG functions are eigenvectors of the Fourier transformation [30]:

$$F\{h_n(t)\} = \lambda_n h_n(t), \tag{6}$$

where F is the Fourier transform operator defined as $F\{s(t)\} = \int s(t) e^{-j2\pi ft} \, dt$ and $\lambda_n = e^{-j\frac{\pi}{2}n}$ is its nth eigenvalue. Similarly, the fractional Fourier transform (FrFT) of order $-2 \leqslant a < 2$, also admits the HG functions as its eigenfunctions [31]:

$$F^a\{h_n(t)\} = e^{-j\frac{\pi}{2}an} h_n(t), \tag{7}$$

where F^a is the FrFT operator of order a. Hence, FrFT of $s(t)$ can be obtained as:

$$F^a\{s(t)\} = \sum_{n=0}^{\infty} \alpha_n e^{-j\frac{\pi}{2}an} h_n(t). \tag{8}$$

As seen from Eq. (7), the FrFT simply scales HGs. Thus, HG functions have circular support in the time–frequency plane. To demonstrate this fact, in Fig. 2, Wigner–Ville distribution of $h_0(t)$, $h_5(t)$, $h_{15}(t)$ and $h_{45}(t)$ are shown.

3. Support adaptive Hermite–Gaussian expansion

A piecewise smooth signal $s(t)$ can be approximated by using the following Lth order HG expansion:

$$\tilde{s}^{(L)}(t) = \sum_{n=0}^{L} \alpha_n h_n(t), \tag{9}$$

with its corresponding normalized approximation error:

$$e^{(L)} = \int |s(t) - \tilde{s}^{(L)}(t)|^2 \, dt \Big/ \int |s(t)|^2 \, dt, \tag{10}$$

where α_n are obtained as in (5). Since the basis functions are orthonormal, in the absence of noise, by increasing the expansion order L, the approximation error can be decreased. However, for
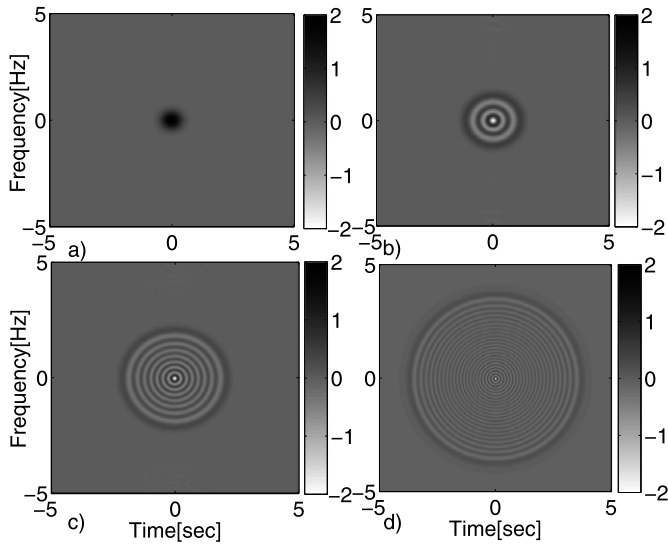
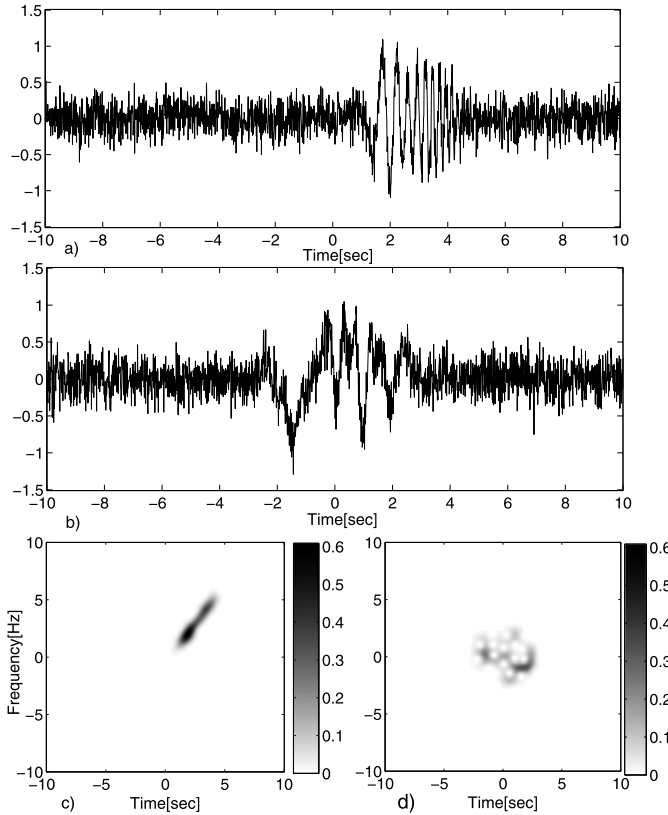**Fig. 2.** Wigner–Ville distribution of (a) $h_0(t)$; (b) $h_5(t)$; (c) $h_{15}(t)$; (d) $h_{45}(t)$.

Fig. 3. Synthetically generated noisy observations of (a) non-circular and (b) circular TFS signals; (c), (d) their respective spectrograms. While computing the spectrograms, a Gaussian window with standard deviation $\sigma = 1/\sqrt{2\pi}$ s was used.

noisy $s(t)$, to avoid noise fitting the expansion order should not be increased indefinitely. Thus, in the noisy case, a low order representation with a reasonably small approximation error is desired. If $s(t)$ has circular TFS centered at the origin of the time–frequency plane, HG basis provides the optimal representation in the sense that the fewest of number of basis functions are required for its representation [25–27]. If $s(t)$ has a non-circular TFS away from the origin, high number of HGs would be used and most of them will have their support largely dominated by noise or other signal components that might be present, rather than the signal component. This fact is demonstrated in Figs. 3 and 4. In Fig. 3, synthet-
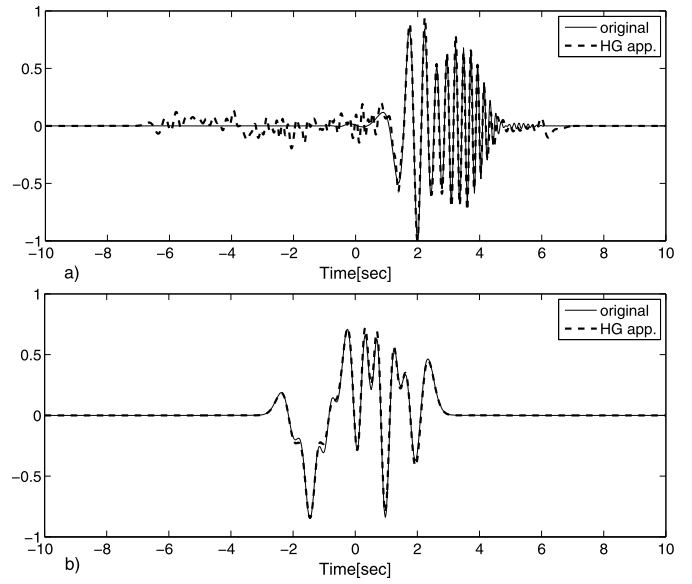

Fig. 4. The original (solid) and HG expansion based approximation (dashed) of the (a) non-circular support and (b) circular support signal shown in Fig. 3.

ically generated noisy observations of non-circular support (a) and circular support (b) signals are shown together with their spectrograms provided in (c) and (d), respectively. In Fig. 4, the actual noise-free signal components and their respective HG approximations are shown. Even at this low SNR, the signal with circular TFS is successfully approximated by HG functions. However, in the case of non-circular support, the representation has significant noise artifacts. Since in practice, TFSs of signal components are not necessarily circular nor centered at the origin, HG representation of them do not provide desirable results. To overcome this problem, we propose a pre-processing stage which transforms the TFS of the signal component to a circular one centered around the origin. This transformation is achieved by applying sequentially three time–frequency operations: (1) time–frequency translation, (2) instantaneous-frequency shifting and (3) scaling. Then, the transformed signal component is represented by HG basis. Finally, obtained representation is transformed back to the original support of the component by applying the corresponding inverse operations as a post-processing stage. In the proceeding subsections, first, proposed operations operating on a mono-component, noise free signal $s(t)$ will be presented. Then, how to apply these operations on noisy observations of multi-component signals will be detailed.

3.1. Time–frequency translation operation

As a first step of support transformation, as in [32], time and frequency centers of a mono-component signal $s(t)$ are obtained by using

$$t_c = \frac{\int t|s(t)|^2\,dt}{\int |s(t)|^2\,dt}, \qquad f_c = \frac{\int f|S(f)|^2\,df}{\int |s(t)|^2\,dt}, \qquad (11)$$

where $S(f)$ is the Fourier transform of $s(t)$. Then, the signal is translated in the time–frequency plane so that its time–frequency center is at the origin:

$$s_c(t) = s(t + t_c)e^{-j2\pi f_c t}. \qquad (12)$$

3.2. Instantaneous frequency shifting operation

To represent $s_c(t)$ with fewest number of HG functions, its TFS should fit into a circular region centered at the origin in

the time–frequency plane. This means that, the generalized time-bandwidth product (GTBP) of the translated signal $s_c(t)$ should be minimized [21]. GTBP of $s_c(t)$ can be minimized by shifting its instantaneous frequency (IF) to the dc level for all time instants. IF of $s_c(t)$ can be computed as

$$f_c(t) = \frac{\int f W_{s_c}(t, f)\, df}{\int W_{s_c}(t, f)\, df}, \tag{13}$$

where $W_{s_c}(t, f)$ is the Wigner–Ville distribution of $s_c(t)$ [32]. Note that since $s_c(t)$ is mono-component and noise free, computed $f_c(t)$ is the true instantaneous frequency of $s_c(t)$. Then, IF shifting operation is applied to $s_c(t)$ as:

$$s_\phi(t) = s_c(t)e^{-j2\pi\phi_c(t)}, \tag{14}$$

where $\phi_c(t)$ is the instantaneous phase of $s_c(t)$ defined as the cumulative IF function [32]:

$$\phi_c(t) = \int_{-\infty}^{t} f_c(\tau)\, d\tau. \tag{15}$$

3.3. Scaling operation

Once time–frequency translation and IF shifting operations are applied to $s(t)$, it should be scaled by a proper scaling factor so that its effective duration and bandwidth are equalized. Effective duration and bandwidth of $s_\phi(t)$ are defined as [32]:

$$D_\phi = \left[\frac{\int (t - t_\phi)^2 |s_\phi(t)|^2\, dt}{\int |s_\phi(t)|^2\, dt}\right]^{1/2}, \tag{16}$$

$$B_\phi = \left[\frac{\int (f - f_\phi)^2 |S_\phi(f)|^2\, df}{\int |s_\phi(t)|^2\, dt}\right]^{1/2}, \tag{17}$$

where $S_\phi(f)$ is the Fourier transform of $s_\phi(t)$, t_ϕ and f_ϕ are, respectively, time and frequency centers of the $s_\phi(t)$ given by

$$t_\phi = \frac{\int t|s_\phi(t)|^2\, dt}{\int |s_\phi(t)|^2\, dt}, \qquad f_\phi = \frac{\int f|S_\phi(f)|^2\, df}{\int |s_\phi(t)|^2\, dt}. \tag{18}$$

Effective duration and bandwidth of $s_\phi(t\nu)$ are equalized by choosing the scaling factor ν as:

$$\nu = \sqrt{D_\phi/B_\phi}. \tag{19}$$

Following this scaling, effective duration and bandwidth of $s_\phi(t\nu)$ are both equal to $\sqrt{D_\phi B_\phi}$. After applying the scaling operation, we get:

$$s_s(t) = s(t\nu + t_c)e^{-j2\pi\phi(t\nu + t_c)}. \tag{20}$$

The effect of the proposed time–frequency operations on the TFS of a mono-component signal is demonstrated in Fig. 5. In (a), TFS of the signal is shown. Here, the radius R effectively determines expansion order for the signal achieving a reasonably small approximation error. After applying (b) time–frequency translation, (c) IF shifting and (d) scaling operations, TFS of the resulting signal fits into a circular region with a smaller area centered around the origin of the time–frequency plane. Since R' is smaller than R, the signal can be represented with significantly less number of basis functions than its original version.

Once these transforms are applied to $s(t)$ as the pre-processing stage, resulting signal $s_s(t)$ is approximated by an Lth order expansion:

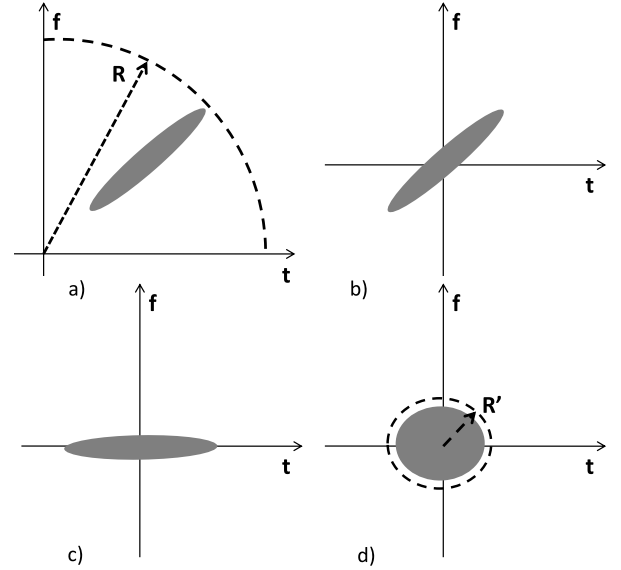$$\tilde{s}_s(t) = \sum_{n=0}^{L} \alpha_n h_n(t), \tag{21}$$

Fig. 5. Illustration of the proposed pre-processing stage: (a) TFS of the signal; (b) after time–frequency translation; (c) after instantaneous frequency shifting; (d) after scaling. R and R' denote the radius of the smallest circle, which encloses the signal support.
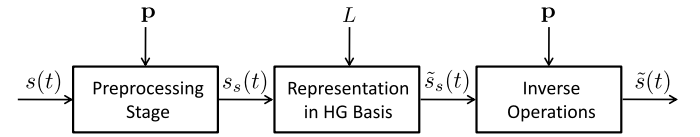

Fig. 6. Support adaptive HG expansion for mono-component signals.

where $\alpha_n = \int h_n(t)s_s(t)\, dt$. Inverse operations are applied to this approximation to obtain an estimate of the original signal $s(t)$:

$$\tilde{s}(t) = \tilde{s}_s\left(\frac{t - t_c}{\nu}\right)e^{j2\pi\phi(t)}. \tag{22}$$

In Fig. 6, block diagram of the proposed support adaptive HG expansion for a mono-component signal $s(t)$ is shown in a compact form. First, pre-processing stage is applied to $s(t)$ to transform its TFS to a circular region centered around the origin. The input $\mathbf{p}$ denotes the parameter vector consisting of the required parameters for the pre-processing stage, i.e., $\mathbf{p} = \{t_c, f(t), \nu\}$. Another important input parameter of the mono-component signal analysis is the representation order L, which will be discussed in detail in Section 4. For a reasonable approximation error, L is chosen according to the area of the effective TFS of $s_s(t)$. Since $s_s(t)$ has compact circular TFS, time-bandwidth product of $s_s(t)$ is a good measure for its TFS [21]. The HG basis expansion in (21) essentially performs a representation of $s_s(t)$ by using $L + 1$ basis functions where $L + 1$, the degrees of freedom in the representation, is approximately same as the time-bandwidth product of $s_s(t)$. Given $\mathbf{p}$ and L, $s_s(t)$ is approximated by $\tilde{s}_s(t)$ as in (21). Then, inverse operations are applied to transform back the support of the obtained signal estimate $\tilde{s}_s(t)$ to its original location.

To demonstrate the performance of the proposed time-frequency transforms, a synthetic mono-component, noise free signal whose real part is shown in Fig. 7(a), was generated. The spectrogram of the signal before and after the pre-processing stage are also provided in (b) and (c), respectively. Note that, the proposed time–frequency operations successfully translate the TFS of the signal to a circular region around the origin. In Fig. 8, we compare the normalized approximation error defined in (10) as
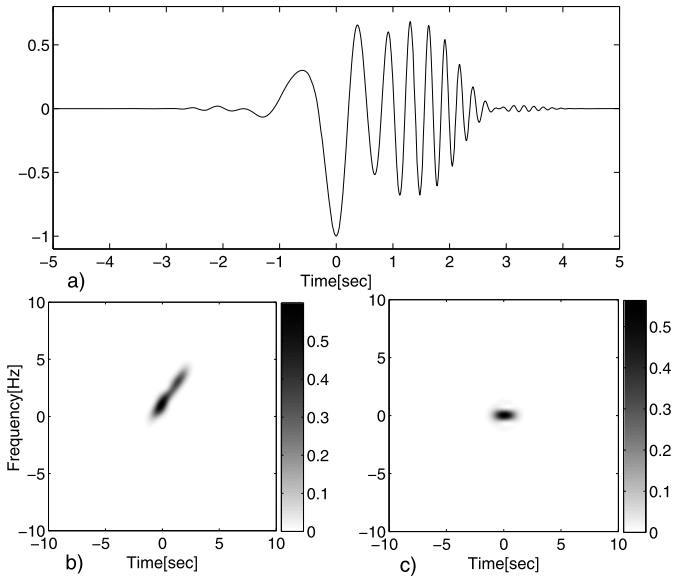
Fig. 7. (a) Synthetically generated signal. Its spectrogram (b) before and (c) after the pre-processing stage. While computing the spectrogram, a Gaussian window with standard deviation $1/\sqrt{2\pi}$ s was used.
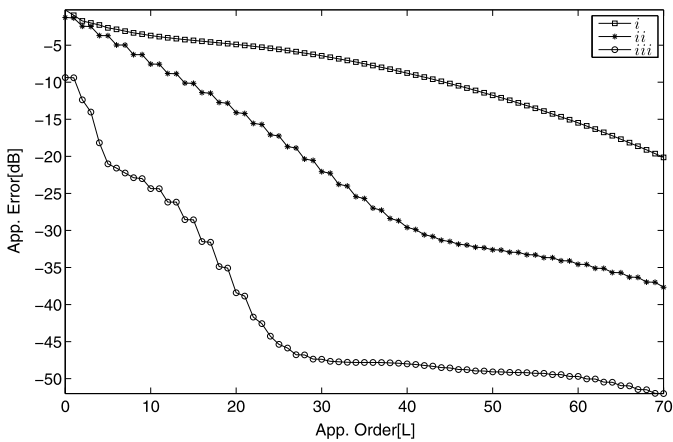

Fig. 8. Normalized approximation error as a function of approximation order L: (i) when no operations is applied (marked with square); (ii) when only time–frequency translation is applied (marked with star); (iii) when all the proposed operations are applied (marked with circle).

a function of approximation order L, (i) when no operations is applied to the signal (marked with squares), (ii) when only time–frequency translation is applied (marked with stars) and (iii) when all the proposed operations are applied (marked with circles). Note that in Fig. 8 approximation order 0 corresponds to the HG representation by using a single HG function of order 0. Therefore, depending on the effectiveness of the pre-processing, the resultant error of the representation eve with a single HG function makes a difference. As illustrated, proposed pre-processing stage significantly decreases the required number of HG functions to achieve a reasonably small approximation error. In Fig. 9, the original signal and its order-10 HG approximation after applying the proposed pre-processing stage are shown for a normalized approximation error of −25 dB. Note that the same level of approximation error would be achieved by using more than 70 basis functions when no pre-processing is performed and more than 35 basis functions when only time–frequency translation is applied.
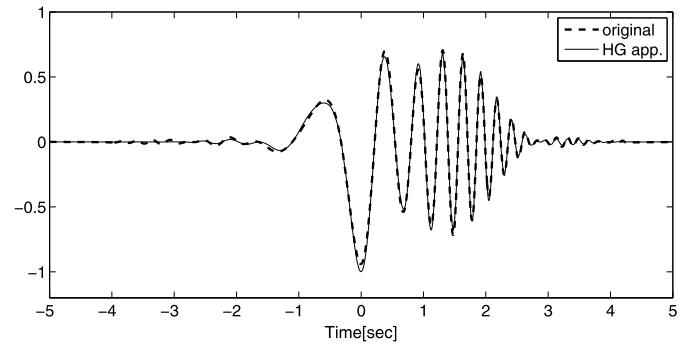

Fig. 9. Comparison of original signal (solid) and order-10 HG approximation (dashed) after applying the proposed pre-processing stage.

4. Iterative component estimation for analysis of multi-component signals

In this section, we discuss the analysis of multi-component signals by using the proposed method. Consider the multi-component signal in noise:

$$x(t) = s_1(t) + s_2(t) + \cdots + s_K(t) + n(t), \tag{23}$$

where $s_k(t)$, $k = 1, 2, \ldots, K$ are signal components with non-overlapping compact TFSs and $n(t)$ is the additive observation noise with variance σ^2, which is assumed to have circularly symmetric white Gaussian distribution. For this multi-component signal, the proposed mono-component analysis technique cannot be applied directly to obtain reliable estimates of the pre-processing stage parameters $\{t_c, f(t), \nu\}$. For estimating each component, the parameters belonging to that particular component should be estimated from the available observation $x(t)$, separately. For this purpose, we propose an EM like iterative, fully automated component estimation technique.

The pre-processing stage parameters for the kth signal component $s_k(t)$ can be estimated from its spectrogram. Since the signal components are assumed to have non-overlapping TFSs, the spectrogram of $s_k(t)$ can be estimated by running a segmentation algorithm on the spectrogram of $x(t)$. At the initialization step $i = 0$ of the proposed iterative technique, the spectrogram of the available observation $|X(t, f)|^2$ is computed, where $X(t, f)$ denotes the short time Fourier transform (STFT) of $x(t)$. While computing the spectrogram, a Gaussian window with a valid variance which resolves all the signal components in the resulting time–frequency distribution is used. This variance can be chosen by observing the time and frequency support of $x(t)$. Let T_x and B_x denote the observed time and frequency support of $x(t)$, respectively. The standard deviation of the Gaussian window for time-bandwidth product optimal STFT is given by $\sqrt{T_x}/\sqrt{2\pi B_x}$ [21]. Then, we use a segmentation algorithm to obtain the initial TFSs of individual signal components. For this purpose, Chan–Vese active contours can be utilized [33]. In this segmentation technique, by minimizing an appropriately chosen energy functional, intensity images are segmented with enclosing contours. Ideally, this energy functional is minimized when the active contours are settled on the boundary of the regions. However, to improve the performance, in [33], authors proposed a variety of user defined stopping criteria for different types of images. In our case, the active contour iterations are terminated when the average intensity along a current contour is larger than a threshold which is chosen as $p_1^i = \lambda^i |X(\bar{t}, \bar{f})|^2 + (1 - \lambda^i)\frac{\sigma^2}{F_s}$, where, σ^2 is the noise variance, F_s is the sampling frequency, $|X(\bar{t}, \bar{f})|^2$ is the maximum value of $|X(t, f)|^2$ and $0 < \lambda^i < 1$ is the parameter controlling the threshold level at iteration i. Here the choice of λ^i is critical, since a very low λ^i may yield a single TFS by combining TFSs

of all the components (occurs more often when the TFSs of the components are close to each other), on the other hand, a very large λ^i may force the segmentation algorithm to miss the TFSs of low amplitude components. After choosing an appropriate λ^i, the segmentation algorithm returns what will be called as initial time–frequency masks $M_k(t, f)$, $k = 1, 2, \ldots, K$ for each component. Then, $\tilde{T}_k(t, f) = X(t, f) \times M_k(t, f)$ serves as an initial estimate for the STFT of $s_k(t)$. Time–frequency translation parameters of the kth component can be estimated from $\tilde{T}_k(t, f)$ by using:

$$\tilde{t}_c^k = \frac{\iint t |\tilde{T}_k(t, f)|^2 \, dt \, df}{\iint |\tilde{T}_k(t, f)|^2 \, dt \, df}, \tag{24}$$

$$\tilde{f}_c^k = \frac{\iint f |\tilde{T}_k(t, f)|^2 \, dt \, df}{\iint |\tilde{T}_k(t, f)|^2 \, dt \, df}. \tag{25}$$

Similarly, IF of $s_k(t)$ can be estimated by:

$$\tilde{f}^k(t) = \frac{\int f |\tilde{T}_k(t, f)|^2 \, df}{\int |\tilde{T}_k(t, f)|^2 \, df}. \tag{26}$$

Once these parameters are estimated, time–frequency translation and IF shifting are applied to the available observation:

$$x_\phi^k(t) = x(t + t_c^k) e^{-j2\pi \phi^k (t + t_c^k)}$$
$$= s_{\phi,k}(t) + \sum_{\substack{h=1 \\ h \neq k}}^{K} s_h(t + t_c^k) e^{-j2\pi \phi^k (t + t_c^k)} + n_\phi^k(t), \tag{27}$$

where $n_\phi^k(t)$ is the resulting noise process and $s_{\phi,k}(t) = s_k(t + t_c^k) \times e^{-j2\pi \phi^k (t + t_c^k)}$. To obtain the scaling factor, STFT of the translated and IF shifted signal component $s_{\phi,k}(t)$ should be estimated. Let $X_\phi^k(t, f)$ denote the STFT of $x_\phi^k(t)$. To obtain an estimate of STFT of $s_{\phi,k}(t)$, one more segmentation is used on $|X_\phi^k(t, f)|^2$ providing more accurate mask $M_{\phi,k}(t, f)$ around the origin by using the segmentation threshold $p_{2,k}^i = \lambda^i |X_\phi^k(\bar{t}, \bar{f})|^2 + (1 - \lambda^i) \frac{\sigma^2}{F_s}$, where $|X_\phi^k(\bar{t}, \bar{f})|^2$ is the maximum value of $|X_\phi^k(t, f)|^2$. By using $M_{\phi,k}(t, f)$, STFT of $s_{\phi,k}(t)$ can be estimated by $\tilde{T}_{\phi,k}(t, f) = X_\phi^k(t, f) \times M_{\phi,k}(t, f)$. Then, effective duration and bandwidth of $s_{\phi,k}(t)$ are obtained from $\tilde{T}_{\phi,k}(t, f)$ by using

$$\tilde{d}_\phi^k = \left[\frac{\iint (t - \tilde{\mu}_t^k)^2 |\tilde{T}_{\phi,k}(t, f)|^2 \, dt \, df}{\iint |\tilde{T}_{\phi,k}(t, f)|^2 \, dt \, df} \right]^{1/2}, \tag{28}$$

$$\tilde{b}_{\phi,k} = \left[\frac{\iint (f - \tilde{\mu}_f^k)^2 |\tilde{T}_{\phi,k}(t, f)|^2 \, dt \, df}{\iint |\tilde{T}_{\phi,k}(t, f)|^2 \, dt \, df} \right]^{1/2}, \tag{29}$$

where $\tilde{\mu}_t^k$ and $\tilde{\mu}_f^k$ are estimates of time and frequency averages:

$$\tilde{\mu}_t^k = \frac{\iint t |\tilde{T}_{\phi,k}(t, f)|^2 \, dt \, df}{\iint |\tilde{T}_{\phi,k}(t, f)|^2 \, dt \, df}, \qquad \tilde{\mu}_f^k = \frac{\iint f |\tilde{T}_{\phi,k}(t, f)|^2 \, dt \, df}{\iint |\tilde{T}_{\phi,k}(t, f)|^2 \, dt \, df}. \tag{30}$$

Since STFT uses a window function, effective duration and bandwidth that are computed over the STFT of the signal are related with the effective duration and bandwidth of the STFT window function through the following equation [32]:

$$d_\phi^k = \sqrt{(D_\phi^k)^2 + D_g^2}, \tag{31}$$

$$b_\phi^k = \sqrt{(B_\phi^k)^2 + B_g^2}. \tag{32}$$

Here, D_ϕ^k and D_g are the true effective durations of $s_\phi^k(t)$ and the STFT window function $g(t)$, respectively, computed using (16).

B_ϕ^k and B_g are the corresponding bandwidths computed using (17). d_ϕ^k and b_ϕ^k are the effective durations and bandwidths of $s_{\phi,k}(t)$ computed over its STFT, $T_{\phi,k}(t, f)$, using (28), (29). Then the scaling factor can be estimated as

$$\tilde{\nu}^k = \sqrt{\frac{(\tilde{d}_\phi^k)^2 - D_g^2}{(\tilde{b}_\phi^k)^2 - B_g^2}}. \tag{33}$$

As $\tilde{T}_{\phi,k}(t, f)$ approaches the true STFT of $s_{\phi,k}(t)$, the estimate in (33) approaches the true scaling parameters $\sqrt{[(d_\phi^k)^2 - D_g^2]/[(b_\phi^k)^2 - B_g^2]}$. After estimating all the transform parameters for all components $\{t_c^k, f^k(t), \nu^k, \ k = 1, 2, \ldots, K\}$ at the initialization step $i = 0$ of the algorithm, the pre-processing stage is applied to the available observation $x(t)$ for each component:

$$x_s^k(t) = x(t\nu^k + t_c^k) e^{-j2\pi \phi^k (t\nu^k + t_c^k)}$$
$$= s_{s,k}(t) + \sum_{\substack{h=1 \\ h \neq k}}^{K} s_h(t\nu^k + t_c^k) e^{-j2\pi \phi^k (t\nu^k + t_c^k)} + n_s^k(t) \tag{34}$$

where $n_s^k(t)$ is the resulting noise process and $s_{s,k}(t) = s_k(t\nu^k + t_c^k) e^{-j2\pi \phi^k (t\nu^k + t_c^k)}$. Note that, after the pre-processing operations, $n_s^k(t)$ is still circularly symmetric Gaussian noise. Then, for estimating each component, its corresponding transformed observation $x_s^k(t)$ is expanded in the HG basis. The expansion coefficients are computed by $\alpha_{n,k} = \int h_n(t) x_s^k(t) \, dt$ and initial estimate of each signal component is computed:

$$\tilde{s}_k^i(t) = \sum_{n=0}^{L_k} \alpha_{n,k} h_n \left(\frac{t - t_c^k}{\nu^k} \right) e^{j2\pi \phi^k(t)}. \tag{35}$$

At this point, assume that the optimal expansion orders L_k, $k = 1, 2, \ldots, K$ are known. At the end of this section, determination of optimal expansion orders will be explained.

Then, we start the EM iterations to further refine the component estimates. This time, for estimating the transform parameters of the kth component, complete information for each component is obtained by the using the following signals: $x_k^{i+1}(t) = x(t) - \sum_{p \neq k} \tilde{s}_p^i(t) \ \forall k = 1, 2, \ldots, K$ is used. The idea is that during the iterations $x_k^{i+1}(t)$ gets closer to a mono-component signal and hence more reliable estimates for the kth component parameters can be obtained. The segmentation algorithm is run over the spectrogram of $x_k^{i+1}(t)$ with a lower threshold parameter $\lambda^{i+1} = \lambda^i c$, where $0 < c < 1$, which is typically chosen as $c = 0.8$, and the transform parameters of the kth component are reestimated from the returned TFS. This parameter estimation process is repeated for all the components before the next EM iteration. The iterations are stopped when the average normalized change in signal estimates between two consecutive EM iterations $\frac{1}{K} \sum_{k=1}^{K} \|\tilde{s}_k^{i+1}(t) - \tilde{s}_k^i(t)\|^2 / \|\tilde{s}_k^{i+1}(t)\|^2$ is lower than a certain threshold q, which is typically chosen as 0.01.

While running the above iterative method, to obtain a reliable estimate of each component, at each iteration, the expansion orders should be chosen optimally. To simplify the notation, we will drop the superscript i, which indicates the iteration number. Since the available observation includes multiple components, the optimal approximation orders $\hat{\mathbf{L}} = [\hat{L}_1, \hat{L}_2, \ldots, \hat{L}_K]$ should be determined jointly so that the identified supports for the components do not have significant overlaps. To determine the optimal approximation orders $\hat{\mathbf{L}}$, the expected value of the total approximation error energy $E\{\int |s(t) - \sum_{k=1}^{K} \tilde{s}_k(t)|^2 \, dt\}$ should be minimized over $\mathbf{L}$. Here, $s(t) = \sum_{k=1}^{K} s_k(t)$ and $\tilde{s}_k(t)$ is the order-L_k HG approximation

of $s_k(t)$ given in (35). To simplify the presentation, we will consider discrete observation case where the bold characters denote the vector of samples of the corresponding continuous time signal. The optimal approximation orders can be estimated by minimizing the following cost function:

$$J(\mathbf{L}) = E\left\{ \left\| \mathbf{s} - \sum_{k=1}^{K} \tilde{\mathbf{s}}_k \right\|^2 \right\}, \tag{36}$$

where $\tilde{\mathbf{s}}_k = \sum_{n=0}^{L_k} \alpha_{n,k} \mathbf{g}_{n,k}$ and representation coefficients $\alpha_{n,k}$ are obtained as $\alpha_{n,k} = \mathbf{h}_n^H \mathbf{x}_s^k$ with $\mathbf{x}_s^k$ being the available observation signal obtained after the pre-processing stage applied for the kth component given in (34). Here, $\mathbf{g}_{n,k}$ is the post-processed HG function of order n for the kth component, specifically, $g_{n,k}(t) = h_n(\frac{t-t_c^k}{\nu^k})e^{j2\pi\phi^k(t)}$, where $\mathbf{h}_n$'s are orthonormalized. Then, the cost function in (36) can be expanded as

$$\begin{aligned} J(\mathbf{L}) &= E\left\{ \mathbf{s}^H \mathbf{s} - 2Re\left\{ \sum_{k=1}^{K} \mathbf{s}^H \tilde{\mathbf{s}}_k \right\} + \sum_{k=1}^{K}\sum_{l=1}^{K} \tilde{\mathbf{s}}_k^H \tilde{\mathbf{s}}_l \right\} \\ &= -2Re\left\{ \sum_{k=1}^{K} E\{\mathbf{s}^H \tilde{\mathbf{s}}_k\} \right\} + \sum_{k=1}^{K} E\{\tilde{\mathbf{s}}_k^H \tilde{\mathbf{s}}_k\} \\ &\quad + \sum_{k=1}^{K}\sum_{l\neq k}^{K} E\{\tilde{\mathbf{s}}_k^H \tilde{\mathbf{s}}_l\}, \end{aligned} \tag{37}$$

where $E\{\mathbf{s}^H \mathbf{s}\}$ term is dropped because it is not a function of $\mathbf{L}$. The first term in (37) can be simplified as:

$$\begin{aligned} Re\left\{ \sum_{k=1}^{K} E\{\mathbf{s}^H \tilde{\mathbf{s}}_k\} \right\} &= Re\left\{ \sum_{k=1}^{K} E\left\{ \mathbf{s}^H \sum_{n=0}^{L_k} \alpha_{n,k} \mathbf{g}_{n,k} \right\} \right\} \\ &= Re\left\{ \sum_{k=1}^{K}\sum_{n=0}^{L_k} E\{\alpha_{n,k}\} \mathbf{s}^H \mathbf{g}_{n,k} \right\} \\ &= Re\left\{ \sum_{k=1}^{K}\sum_{n=0}^{L_k} E\{\mathbf{h}_n^H \mathbf{x}_s^k\} \mathbf{s}^H \mathbf{g}_{n,k} \right\} \\ &= Re\left\{ \sum_{k=1}^{K}\sum_{n=0}^{L_k} E\{\mathbf{h}_n^H (\mathbf{s}_s^k + \mathbf{n}_s^k)\} \mathbf{s}^H \mathbf{g}_{n,k} \right\}. \end{aligned} \tag{38}$$

Since $\mathbf{n}_s^k$ is zero mean,

$$\begin{aligned} Re\left\{ \sum_{k=1}^{K} E\{\mathbf{s}^H \tilde{\mathbf{s}}_k\} \right\} &= Re\left\{ \sum_{k=1}^{K}\sum_{n=0}^{L_k} \mathbf{h}_n^H \mathbf{s}_s^k \mathbf{s}^H \mathbf{g}_{n,k} \right\} \\ &= Re\left\{ \sum_{k=1}^{K}\sum_{n=0}^{L_k} \beta_{n,k} \beta_{n,k}^* \nu^k \right\} \\ &= \sum_{k=1}^{K}\sum_{n=0}^{L_k} \nu^k |\beta_{n,k}|^2. \end{aligned} \tag{39}$$

Here, $\mathbf{s}_s^k$ and $\mathbf{n}_s^k$ are the sum of the signal components and noise after the pre-processing stage applied for the kth component in (34) respectively, i.e., $s_s^k(t) = s(t\nu^k + t_c^k)e^{-j2\pi\phi^k(t\nu^k+t_c^k)}$, and $n_s^k(t) = x_s^k(t) - s_s^k(t)$. The coefficient $\beta_{n,k}$ is the projection of $s_s^k(t)$ on the nth HG function, i.e., $\beta_{n,k} = \mathbf{h}_n^H \mathbf{s}_s^k$, and $\mathbf{s}^H \mathbf{g}_{n,k} = \beta_{n,k}^*$ since $\int h_n(t)^* s_s(t)\,dt = \frac{1}{\nu^k} \int g_{n,k}(t)^* s(t)\,dt$. Note that pre-processing stage doesn't change the statistical properties of the noise process, which

is assumed to have a circularly symmetric white Gaussian distribution with variance σ^2. The expectation in the second term in (37) can be computed as:

$$\sum_{k=1}^{K} E\{\tilde{\mathbf{s}}_k^H \tilde{\mathbf{s}}_k\} = \sum_{k=1}^{K} E\left\{ \left(\sum_{n=0}^{L_k} \alpha_{n,k} \mathbf{g}_{n,k} \right)^H \left(\sum_{m=0}^{L_k} \alpha_{m,k} \mathbf{g}_{m,k} \right) \right\}. \tag{40}$$

Since $\mathbf{g}_{n,k}^H \mathbf{g}_{m,k} = \nu^k \delta(m-n)$, it reduces to

$$\begin{aligned} \sum_{k=1}^{K} E\{\tilde{\mathbf{s}}_k^H \tilde{\mathbf{s}}_k\} &= \sum_{k=1}^{K} E\left\{ \sum_{n=0}^{L_k} \nu^k |\alpha_{n,k}|^2 \right\} \\ &= \sum_{k=1}^{K}\sum_{n=0}^{L_k} \nu^k E\{\mathbf{h}_n^H \mathbf{x}_s^k \mathbf{x}_s^{k^H} \mathbf{h}_n\} \\ &= \sum_{k=1}^{K}\sum_{n=0}^{L_k} \nu^k \mathbf{h}_n^H E\{ (\mathbf{s}_s^k + \mathbf{n}_s^k)(\mathbf{s}_s^k + \mathbf{n}_s^k)^H \} \mathbf{h}_n. \end{aligned} \tag{41}$$

Since $\mathbf{n}_s^k$ is circularly symmetric white Gaussian noise,

$$\begin{aligned} \sum_{k=1}^{K} E\{\tilde{\mathbf{s}}_k^H \tilde{\mathbf{s}}_k\} &= \sum_{k=1}^{K}\sum_{n=0}^{L_k} \nu^k \mathbf{h}_n^H [\mathbf{s}_s^k \mathbf{s}_s^{k^H} + \sigma^2 \mathbf{I}] \mathbf{h}_n \\ &= \sum_{k=1}^{K}\sum_{n=0}^{L_k} \nu^k |\beta_{n,k}|^2 + \sum_{k=1}^{K} \nu^k (L_k+1)\sigma^2, \end{aligned} \tag{42}$$

where $\mathbf{I}$ is the identity matrix. Finally, the expectation in the third term in (37) can be computed as:

$$\begin{aligned} \sum_{k=1}^{K}\sum_{l\neq k}^{K} E\{\tilde{\mathbf{s}}_k^H \tilde{\mathbf{s}}_l\} &= \sum_{k=1}^{K}\sum_{l\neq k}^{K} E\left\{ \left(\sum_{n=0}^{L_k} \alpha_{n,k}^* \mathbf{g}_{n,k}^H \right) \left(\sum_{m=0}^{L_l} \alpha_{m,l} \mathbf{g}_{m,l} \right) \right\} \\ &= \sum_{k=1}^{K}\sum_{l\neq k}^{K}\sum_{n=0}^{L_k}\sum_{m=0}^{L_l} E\{\alpha_{n,k}^* \alpha_{m,l}\} \xi_{n,k}^{n,l}, \end{aligned} \tag{43}$$

where $\xi_{n,k}^{m,l} = \mathbf{g}_{n,k}^H \mathbf{g}_{m,l}$. Then,

$$\begin{aligned} &\sum_{k=1}^{K}\sum_{l\neq k}^{K} E\{\tilde{\mathbf{s}}_k^H \tilde{\mathbf{s}}_l\} \\ &= \sum_{k=1}^{K}\sum_{l\neq k}^{K}\sum_{n=0}^{L_k}\sum_{m=0}^{L_l} E\{\mathbf{h}_m^H \mathbf{x}_s^l \mathbf{x}_s^{k^H} \mathbf{h}_n\} \xi_{n,k}^{m,l} \\ &= \sum_{k=1}^{K}\sum_{l\neq k}^{K}\sum_{n=0}^{L_k}\sum_{m=0}^{L_l} \mathbf{h}_m^H E\{ (\mathbf{s}_s^l + \mathbf{n}_s^l)(\mathbf{s}_s^k + \mathbf{n}_s^k)^H \} \mathbf{h}_n \xi_{n,k}^{m,l} \\ &= \sum_{k=1}^{K}\sum_{l\neq k}^{K}\sum_{n=0}^{L_k}\sum_{m=0}^{L_l} \mathbf{h}_m^H (\mathbf{s}_s^l \mathbf{s}_s^{k^H} + \sigma^2 \mathbf{I}) \mathbf{h}_n \xi_{n,k}^{m,l}. \end{aligned} \tag{44}$$

Since $\mathbf{h}_m^H \mathbf{h}_n = \delta(m-n)$,

$$\begin{aligned} \sum_{k=1}^{K}\sum_{l\neq k}^{K} E\{\tilde{\mathbf{s}}_k^H \tilde{\mathbf{s}}_l\} &= \sum_{k=1}^{K}\sum_{l\neq k}^{K}\sum_{n=0}^{L_k}\sum_{m=0}^{L_l} \beta_{m,l} \beta_{n,k}^* \xi_{n,k}^{m,l} \\ &\quad + \sigma^2 \sum_{k=1}^{K}\sum_{l\neq k}^{K}\sum_{n=0}^{\min\{L_k,L_l\}} \xi_{n,k}^{n,l}. \end{aligned} \tag{45}$$

Then Eq. in (36) reduces to the following form:

$$J(\mathbf{L}) = -\sum_{k=1}^{K}\sum_{n=0}^{L_k} \nu^k |\beta_{n,k}|^2 + \sum_{k=1}^{K} \nu^k (L_k + 1)\sigma^2$$
$$+ \sum_{k=1}^{K}\sum_{l \neq k}^{K}\sum_{n=0}^{L_k}\sum_{m=0}^{L_l} \beta_{m,l}\beta_{n,k}^* \xi_{n,k}^{m,l}$$
$$+ \sigma^2 \sum_{k=1}^{K}\sum_{l \neq k}^{K}\sum_{n=0}^{\min\{L_k,L_l\}} \xi_{n,k}^{n,l}. \qquad (46)$$

However, since we do not have access to the noise free signal $s(t)$, $\beta_{n,k}$ cannot be computed directly. However, as detailed in the next derivation, $|\beta_{n,k}|^2 \approx |\alpha_{n,k}|^2 - \sigma^2$. This is because $E\{|\alpha_{n,k}|^2\} = |\beta_{n,k}|^2 + \sigma^2$.

$$E\{|\alpha_{n,k}|^2\} = E\{\mathbf{h}_n^H \mathbf{x}_s^k \mathbf{x}_s^{k^H} \mathbf{h}_n\}$$
$$= \mathbf{h}_n^H E\{\mathbf{x}_s^k \mathbf{x}_s^{k^H}\} \mathbf{h}_n$$
$$= \mathbf{h}_n^H E\{(\mathbf{s}_s^k + \mathbf{n}_s^k)(\mathbf{s}_s^k + \mathbf{n}_s^k)^H\} \mathbf{h}_n$$
$$= \mathbf{h}_n^H (\mathbf{s}_s^k \mathbf{s}_s^{k^H} + \sigma^2 \mathbf{I}) \mathbf{h}_n$$
$$= |\beta_{n,k}|^2 + \sigma^2. \qquad (47)$$

By using this approximation, the following computable cost function, which is to be minimized, is used in the proposed approach here:

$$\hat{J}(\mathbf{L}) = -\sum_{k=1}^{K}\sum_{n=0}^{L_k} \nu^k |\alpha_{n,k}|^2 + 2\sum_{k=1}^{K} \nu^k (L_k + 1)\sigma^2$$
$$+ \sum_{k=1}^{K}\sum_{l \neq k}^{K}\sum_{n=0}^{L_k}\sum_{m=0}^{L_l} \alpha_{n,k}^* \alpha_{m,l} \xi_{n,k}^{m,l}. \qquad (48)$$

In the above cost function, while the second term controls the effect of noise, third term controls the cross correlation between the signal estimates. For mono-component case $K = 1$, the cost function in (48) reduces to

$$\hat{J}(\mathbf{L})_{K=1} = -\sum_{n=0}^{L} \nu^1 |\alpha_{n,1}|^2 + 2\nu^1 (L + 1)\sigma^2. \qquad (49)$$

To simulate the performance of the expansion order estimator for mono-component signals given in (49), we generated ten thousand different realizations of a noisy synthetic signal of the form $x(t) = \sum_{n=0}^{\bar{L}} \alpha_n h_n(t) + n(t)$. In each realization, the HG coefficients α_n, $n = 0, 1, \ldots, \bar{L}$ were chosen from a normal distribution and the noise samples $n(t)$ were generated from a zero mean Gaussian distribution, whose variance was set according to the given SNR value. For different representation orders $\bar{L}$ (ranging from 0 to 100), and different SNR values (ranging from -10 dB to 10 dB), we calculated the sample mean and sample standard deviation of the absolute error between the actual representation order $\bar{L}$ and its estimate $\tilde{L}$, i.e. $|\bar{L} - \tilde{L}|$. In Figs. 10(a) and (b), these two statistical measures are plotted as a function of $\bar{L}$ for different SNR values. As observed from this plot, even for a complicated signal that is composed of many HGs (e.g. $L = 100$) and under very low SNR values (e.g. -10 dB), the average absolute error in expansion order estimation is only around 3.5 with standard deviation of 5.5.

Having discussed choosing the expansion orders optimally, the fully automated iterative method for signal component estimation is summarized in Algorithm 1.

When the signal components have overlapping TFSs, decomposing the observation signal into its components is a harder problem.
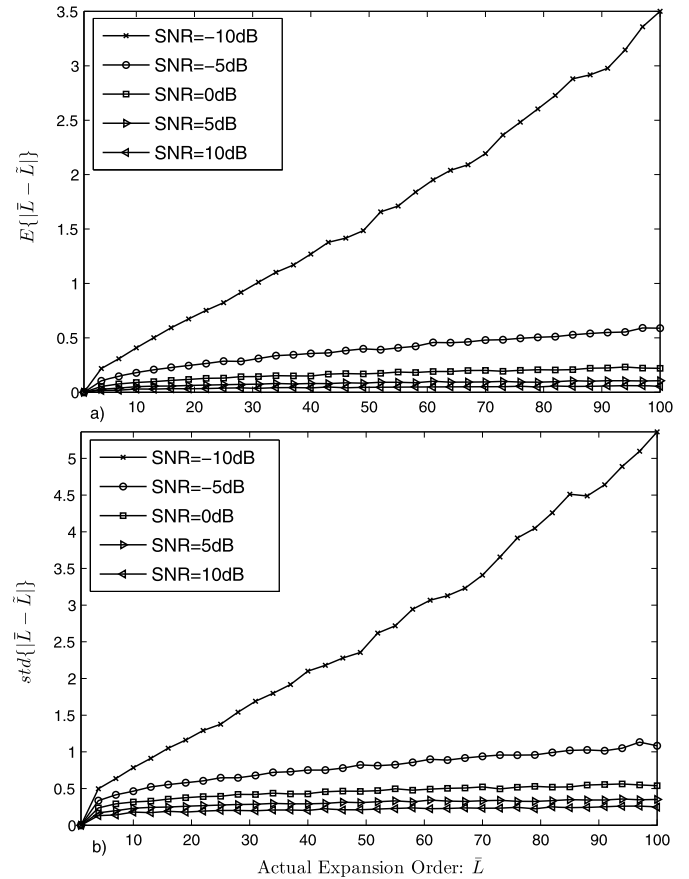

Fig. 10. (a) Ensemble average of the absolute error between actual representation order $\bar{L}$ and its estimate $\tilde{L}$ and (b) its standard deviation as a function of $\bar{L}$ for different SNR values.

Although the proposed approach is designed for analysis of signals whose time–frequency components do not have significant overlaps in the time–frequency domain, some insights for the overlapping case will be provided. Consider a signal $s(t)$, which have two components with overlapping TFSs $s(t) = s_1(t) + s_2(t)$, as demonstrated in Fig. 11. In the figure, S_1 and S_2 denote the effective TFS of $s_1(t)$ and $s_2(t)$, respectively. S_{int} is the effective support of the overlap region. Let $\mathbb{S}[.]$ be an operator which returns the effective support of the given signal, i.e., $\mathbb{S}[s_k(t)] = S_k$, $k = 1, 2$, and H_0 denote the effective support of HG function of order 0, i.e., $\mathbb{S}[h_0(t)] = H_0$. The following two theorems explain the uniqueness of the decomposition of $s(t)$ into $s_1(t)$ and $s_2(t)$ according to the area of the effective intersection region between the component supports.

Theorem 1. *If the intersection region S_{int} allows covering an ellipse of area larger than or equal to the area of H_0, the decomposition $s(t) = \tilde{s}_1(t) + \tilde{s}_2(t)$ such that $\mathbb{S}[\tilde{s}_1(t)] = S_1$ and $\mathbb{S}[\tilde{s}_1(t)] = S_2$ is non-unique.*

Proof. Since area of S_{int} is larger than H_0, there exist a signal $s_{int}(t)$ with a sufficiently small energy such that $\mathbb{S}[s_{int}(t)] \subseteq S_{int}$. The decomposition can be rewritten as

$$s(t) = \tilde{s}_1(t) + \tilde{s}_2(t)$$
$$= \tilde{s}_1(t) + \tilde{s}_2(t) + s_{int}(t) - s_{int}(t)$$
$$= \tilde{s}_1(t) + s_{int}(t) + \tilde{s}_2(t) - s_{int}(t). \qquad (50)$$

Algorithm 1 Component extraction based on iterative parameter estimation.

```
1: //Initialization
2: i ← 0
3: Set segmentation threshold parameter λⁱ
4: Set segmentation threshold p₁ⁱ = λⁱ|X(t̄, f̄)|² + (1 − λⁱ)σ²/Fₛ
5: Estimate tᶜᵏ, fᵏ(t) ∀k = 1, 2, …, K by segmenting |X(t, f)|² with the segmenta-
   tion threshold p₁ⁱ
6: Compute x_φᵏ(t) ∀k = 1, 2, …, K by using tᶜᵏ, fᵏ(t)
7: Set segmentation threshold p₂,ₖⁱ = λⁱ|X_φᵏ(t̄, f̄)|² + (1 − λⁱ)σ²/Fₛ ∀k = 1, 2, …, K
8: Estimate νᵏ ∀k = 1, 2, …, K by segmenting |X_φᵏ(t, f)|² with the segmentation
   threshold p₂,ₖⁱ
9: Form x_sᵏ(t) ∀k = 1, 2, …, K
10: Compute αₙ,ₖ, ξₙ,ₖᵐ,ˡ ∀k, l = 1, 2, …, K, ∀n, m = 1, 2, ..
11: Solve (48) using {αₙ,ₖ, ξₙ,ₖᵐ,ˡ, νᵏ, ∀k, l = 1, 2, …, K, ∀n, m = 1, 2, ..}
12: Compute s̃ₖⁱ(t), ∀k = 1, 2, …, K
13: qⁱ = 1
14: //EM Iterations
15: while qⁱ > q do
16:    i ← i + 1
17:    λⁱ = cλⁱ⁻¹
18:    for k = 1 to K do
19:       xₖⁱ(t) ← x(t) − Σ_{p≠k} s̃ₚⁱ⁻¹(t)
20:       Set segmentation threshold p₁ⁱ = λⁱ|Xₖ(t̄, f̄)|² + (1 − λⁱ)σ²/Fₛ
21:       Estimate tᶜᵏ, fᵏ(t) by segmenting |Xᵏ(t, f)|² with the segmentation
          threshold p₁ⁱ
22:       Compute x_φᵏ(t) by using tᶜᵏ, fᵏ(t)
23:       Set segmentation threshold p₂ⁱ = λⁱ|X_φᵏ(t̄, f̄)|² + (1 − λⁱ)σ²/Fₛ
24:       Estimate νᵏ by segmenting |X_φᵏ(t, f)|² with the segmentation threshold
          p₂ⁱ
25:    end for
26:    Form x_sᵏ(t) ∀k = 1, 2, …, K
27:    Compute αₙ,ₖ, ξₙ,ₖᵐ,ˡ ∀k, l = 1, 2, …, K, ∀n, m = 1, 2, ..
28:    Solve (48) using {αₙ,ₖ, ξₙ,ₖᵐ,ˡ, νᵏ, ∀k, l = 1, 2, …, K, ∀n, m = 1, 2, ..}
29:    Compute s̃ₖⁱ(t), ∀k = 1, 2, …, K
30:    qⁱ = (1/K) Σ_{k=1}^{K} ‖s̃ₖⁱ(t) − s̃ₖⁱ⁻¹(t)‖²/‖s̃ₖⁱ(t)‖²
31: end while
```
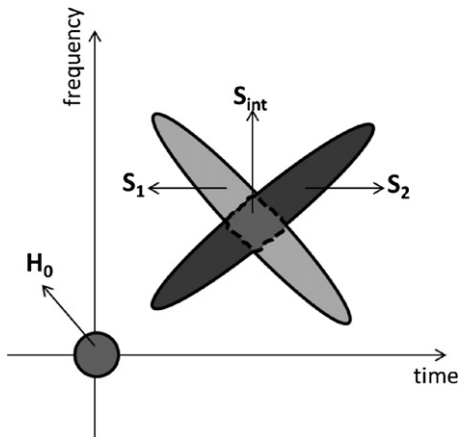

Fig. 11. Demonstration of a multi-component signal whose components have overlapping TFSs. S_1 and S_2 are the effective TFSs of the signal components. S_{int} is the effective overlapping region. H_0 denotes the effective TFS of the HG function of order 0.

Since $\mathbb{S}[\tilde{s}_1(t) + s_{int}(t)] = S_1$ and $\mathbb{S}[\tilde{s}_2(t) - s_{int}(t)] = S_2$, $s(t) = [\tilde{s}_1(t) + s_{int}(t)] + [\tilde{s}_2(t) - s_{int}(t)]$ is another decomposition of $s(t)$. Hence, the decomposition is non-unique.

Theorem 2. *If the intersection region S_{int} doesn't allow covering an ellipse of area larger than or equal to the area of H_0, the decomposition $s(t) = \tilde{s}_1(t) + \tilde{s}_2(t)$ such that $\mathbb{S}[\tilde{s}_1(t)] = S_1$ and $\mathbb{S}[\tilde{s}_2(t)] = S_2$ is unique.*

Proof. Assume that there exists non-unique decompositions $s(t) = \tilde{s}_1(t) + \tilde{s}_2(t)$ and $s(t) = \hat{s}_1(t) + \hat{s}_2(t)$. Then,

$$
\begin{aligned}
0 &= \tilde{s}_1(t) + \tilde{s}_2(t) - \hat{s}_1(t) - \hat{s}_2(t) \\
&= \left[\tilde{s}_1(t) - \hat{s}_1(t)\right] + \left[\tilde{s}_2(t) - \hat{s}_2(t)\right] \\
&= e_1(t) + e_2(t),
\end{aligned}
\tag{51}
$$

where $e_1(t) = \tilde{s}_1(t) - \hat{s}_1(t)$ and $e_2(t) = \tilde{s}_2(t) - \hat{s}_2(t)$. Since $e_1(t) + e_2(t) = 0$, then $\mathbb{S}[e_1(t)] = \mathbb{S}[e_2(t)]$. Therefore, $\mathbb{S}[e_1(t)] \subset S_{int}$ and $\mathbb{S}[e_2(t)] \subset S_{int}$. This is a contradiction since it is already assumed that area of S_{int} is smaller than H_0 and there exists no signal whose effective TFS is equal to S_{int}. Hence the decomposition is unique. $\square$

In Theorem 1, it is proven that, if the overlapped region between two signal components has an area of larger than or equal to the effective support of a Gaussian atom (Hermite–Gaussian function of order 0), then the unique separation of these two components is not possible. Therefore, there exist no time–frequency analysis tools that can uniquely decompose overlapping components whenever their overlapped region is sufficiently large. Theorem 2 provides a positive result for the analysis of overlapping signal components. It states that if the overlapped area doesn't allow fitting a Gaussian atom, then the decomposition becomes unique. To extend the proposed approach to the case of overlapping signal components as described in Theorem 2, the proposed approach can be modified such that Hermite–Gaussian fitting is performed in the non-overlapping parts of the signal components after the pre-processing stage. However this extension of the proposed approach is left as a future work on the subject.

In the next section, analysis results on both simulated and real signals will be provided.

5. Analysis of results on simulated and real signals

To demonstrate the performance of the proposed method, we conducted experiments on synthetically generated mono- and multi-component signals. For the mono-component case, the noisy observation of a compact support signal of the form:

$$
s(t) = w(t; t_1, t_2)a(t)e^{-j2\pi(\alpha t^2 + \beta t + \gamma)}
\tag{52}
$$

was generated. Here $a(t)$ is low-pass filtered circularly symmetric white noise, $\{\alpha, \beta, \gamma\}$ are IF parameters imposing linear frequency modulation to the signal. As shown in Fig. 12, $w(t)$ is the time-window:

$$
w(t; t_1, t_2) = \begin{cases} e^{-(t-t_1)^2/\kappa^2} & \text{if } t < t_1, \\ 1 & \text{if } t_1 \leqslant t \leqslant t_2, \\ e^{-(t-t_2)^2/\kappa^2} & \text{if } t > t_2, \end{cases}
\tag{53}
$$

forcing the signal to have a compact TFS. The noise variance was chosen such that the SNR was set to 0 dB, which is defined as $\text{SNR} = 10 \log \|\mathbf{s}\|^2/(N_s\sigma^2)$ where N_s is the number of available samples along the signal support and σ^2 is the noise variance. The spectrograms of the available signal before and after the pre-processing stage are also provided in Figs. 12(b) and (c), respectively. In a fully automated fashion, all the required parameters are estimated using signal support returned by the segmentation algorithm. In Fig. 13, approximation error as a function of expansion order is plotted. As seen from this figure, if HG projections are directly applied to the signal without applying the proposed pre-processing technique (marked with squares), approximation error remains above −10 dB. If only time–frequency translation is applied (marked with stars), the lowest approximation error achieved is around −13 dB and corresponding approximation order is 35.
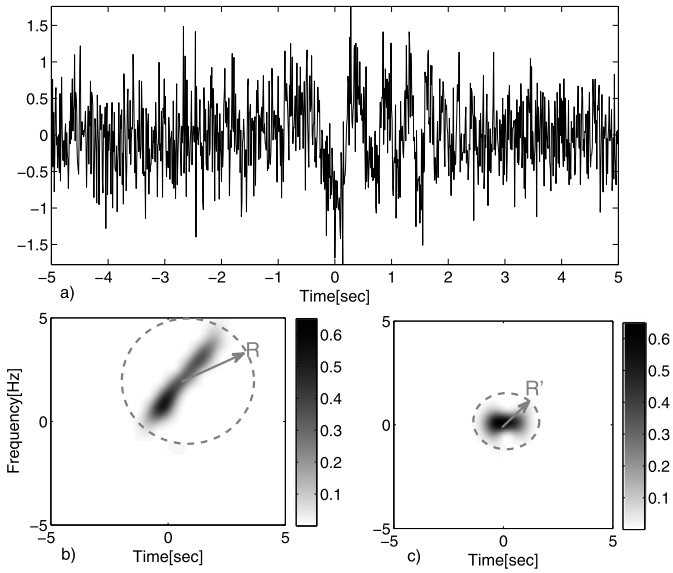
Fig. 14. (a) Sym8 wavelet and (b) its corresponding scaling function.

Fig. 12. (a) Synthetically generated noisy observation of a mono-component, compact TFS signal. SNR is 0 dB. Its spectrogram (b) before and (c) after pre-processing stage. R and R' represent the radius of the smallest circle that encloses the signal support. While computing the spectrograms, a Gaussian window with standard deviation $\sigma = 1/\sqrt{2\pi}$ s was used.
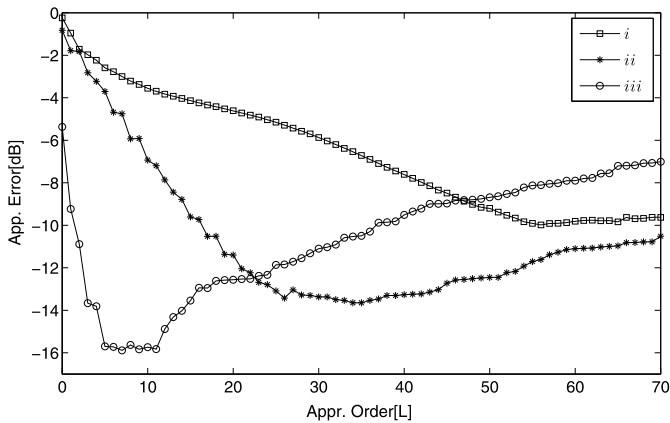

Fig. 15. Original signal (solid-black), its approximation by proposed method (dashed-blue) and wavelet soft-thresholding technique (dashed-doted-red). (For interpretation of the references to color in this figure legend, the reader is referred to the web version of this article.)

Fig. 13. Approximation error as a function of approximation order: (i) if no transform is applied (marked with squares); (ii) if only time–frequency translation is applied (marked with stars); (iii) if all the proposed transforms are applied (marked with circles).

If full scale pre-processing is applied (marked with circles), the lowest approximation error achieved is around -16 dB and the corresponding expansion order is only 7. For this synthetic signal, we compared the performance of the proposed method with the powerful wavelet soft-thresholding technique [34]. First, discrete wavelet transform is applied to the available observation and wavelet coefficients ξ_k, $k = 0, 1, 2..., N$ (N is the number of available samples) were obtained. We used Daubechies' compactly supported, nearly linear phase wavelet *sym8* with 9 vanishing moments [35]. The *sym8* wavelet and its scaling function are shown in Fig. 14. Then, soft thresholding is applied to the wavelet coefficients $\hat{\xi}_k$ as:

$$\hat{\xi}_k = \mathrm{sgn}(\xi_k)\big(|\xi_k| - \hat{\epsilon}\big)_+, \tag{54}$$

where $(.)_+$ is the non-negative part of its argument and the denoised signal was reconstructed by applying the inverse wavelet transform to the new coefficients. The threshold $\hat{\epsilon}$ was estimated according to Stein's unbiased estimate of risk [36]:
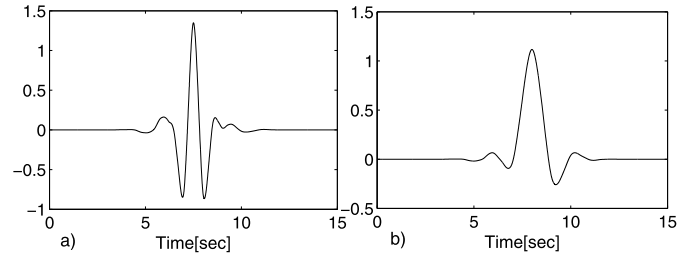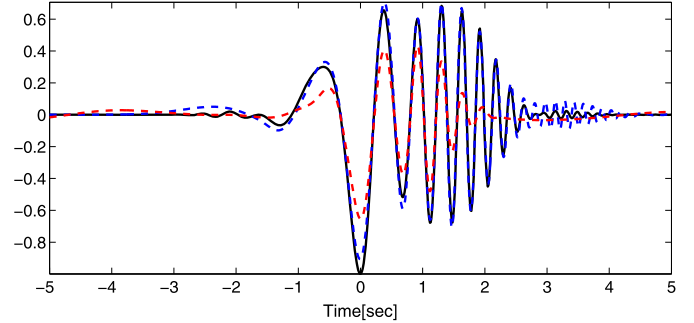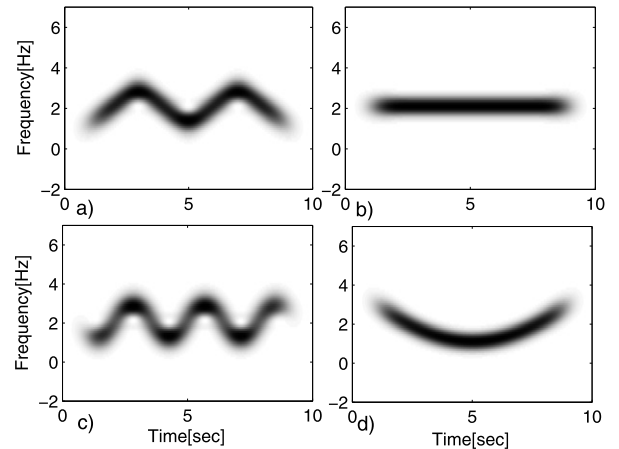

Fig. 16. Spectrogram of the synthetic test signals with (a) triangular, (b) constant, (c) sinusoidal and (d) quadratic instantaneous frequencies.

$$\hat{\epsilon} = \underset{0 \leqslant \epsilon \leqslant \sqrt{2\log N}}{\arg\min} \left[N - 2\big\{k\colon |\xi_k| \leqslant \epsilon|\big\} + \sum_{k=1}^{N} \min\big(|\xi_k|, \epsilon\big) \right]. \tag{55}$$

In Fig. 15, the original signal component (solid-black), its approximation by the proposed method (dashed-blue) and the wavelet soft-thresholding technique (dashed-dotted-red) are plotted. For the proposed method, the optimal expansion order is estimated by using (49) to be 5, which is consistent with Fig. 13. While the proposed method achieves an approximation error of -15.2 dB, the approximation error of the wavelet shrinkage technique remains around -6.8 dB. As observed from this figure, although the available observations are significantly noisy, the proposed technique provides accurate estimates for the signal component. To provide more comparison results of the proposed method with wavelet soft-thresholding technique, four more synthetic signals with triangular, constant, sinusoidal and quadratic instantaneous frequencies were generated. Spectrogram of each test signal is shown in Fig. 16. For different SNR values, approximation errors of both

Table 1
Approximation errors of the proposed method (Prop. Meth.) and wavelet soft-thresholding (W.S. Thres.) for the test signals with triangular (Trian.), constant (Cons.), sinusoidal (Sin.) and quadratic (Quad.) instantaneous frequencies shown in Fig. 16, for different SNR values.

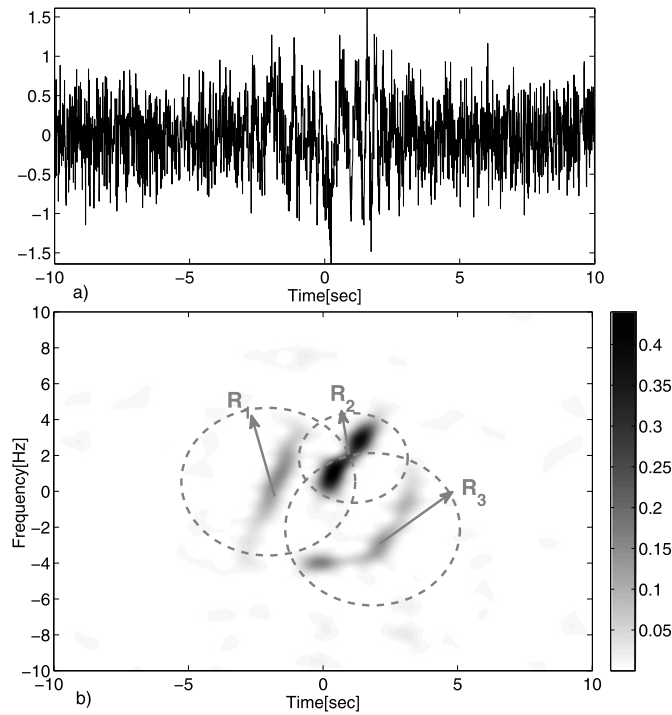|		Trian.	Cons.	Sin.	Quad.
SNR = 0 dB	Prop. Meth.	−13.6	−14.9	−14.6	−12.8
SNR = 0 dB	W.S. Thres.	−9.1	−10.5	−7.9	−9.8
SNR = 5 dB	Prop. Meth.	−17.6	−19.4	−15.6	−15.8
SNR = 5 dB	W.S. Thres.	−9.8	−12.8	−9	−11.6

Fig. 17. (a) Synthetically generated noisy observation of a 3-component signal and (b) its spectrogram. SNR is 0 dB. R_1, R_2, R_3 represent the radius of the smallest circle that encloses the support of the first, second and third component, respectively. While computing the spectrogram, a Gaussian window with standard deviation $\sigma = 1/\sqrt{2\pi}$ s was used.
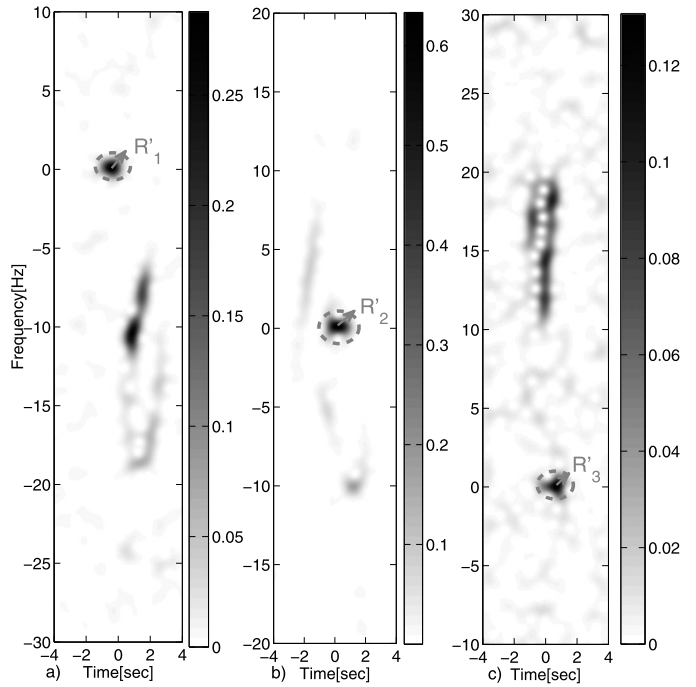

Fig. 18. Spectrogram of the signal shown in Fig. 17 after applying pre-processing stage by using the parameters of the (a) first, (b) second and (c) third component. R'_1, R'_2, R'_3 represent the radius of the smallest circle that encloses the support of the first, second and third component after the corresponding transformation. While computing the spectrograms, a Gaussian window with standard deviation $\sigma = 1/\sqrt{2\pi}$ s was used.
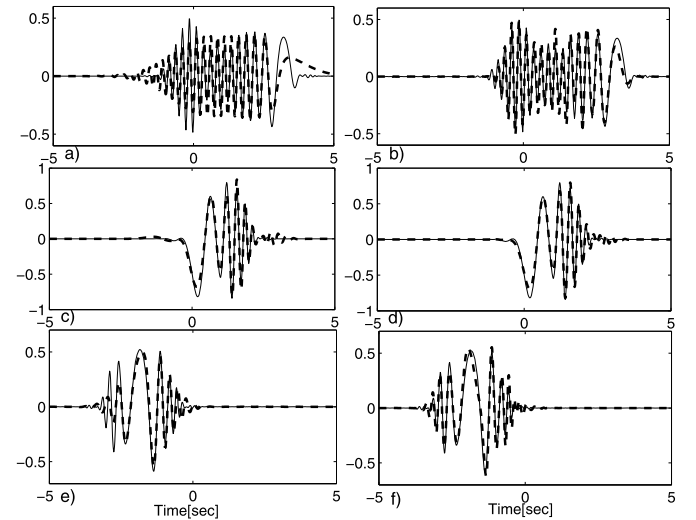

Fig. 19. Actual (solid) and estimated (dashed) components at the end of the (a), (c), (e) 1th and (b), (d), (f) 15th iteration of Algorithm 1.

methods are reported in Table 1. Proposed method achieved a significantly lower approximation error for each test case.

For the multi-component scenario, a three-component signal is used. In this case, linear frequency modulation was imposed on the first and the second components and quadratic frequency modulation was imposed on the third component. The noisy signal and its spectrogram are shown in Figs. 17(a) and (b), respectively. Since TFSs of the components are close to each other in the time–frequency plane, projecting the observation signal on even the time–frequency translated HGs cannot yield reliable component estimates. As demonstrated in Fig. 17(b), for each component, there is some energy leaked from the others in the region defined by the smallest circle that encloses the support of that particular component. After applying the pre-processing stage to the observation signal given in Fig. 17 for each component separately, the spectrogram of the resulting signals are shown in Fig. 18. Note that the radii of the smallest circles that enclose the TFSs of the components in the resulting signal R'_1, R'_3, R'_3 are considerably smaller compared to R_1, R_2, R_3 shown in Fig. 17, decreasing the required number of HGs in the representation of the signal and hence decreasing the amount of noise fitting in the representation.

To demonstrate the performance of the proposed method on multi-component signals, synthetic signal shown in Fig. 17 was used. For approximating each component Algorithm 1 was de-

ployed. After 15 iterations, Algorithm 1 terminated. In Figs. 19(a), (c), (e), estimated components and the actual ones at the end of the first iteration of Algorithm 1 are shown. Especially, for the low amplitude components (a) and (c), approximation error is high. In (b), (d), (f), results at the end of the last iteration are given. The approximation errors of the first iteration are highly reduced. Since all the signal components are detected by running Chan–Vese segmentation algorithm on the spectrogram of the available observation and all required parameters are estimated from the detected component supports, proposed method is a fully automated procedure.

The effect of the incorporated segmentation technique is also investigated in the multi-component signal given in Fig. 17. For

Table 2
Normalized approximation error and energy difference for each component estimated by utilizing Chan–Vese and Watershed segmentation techniques in the proposed method.

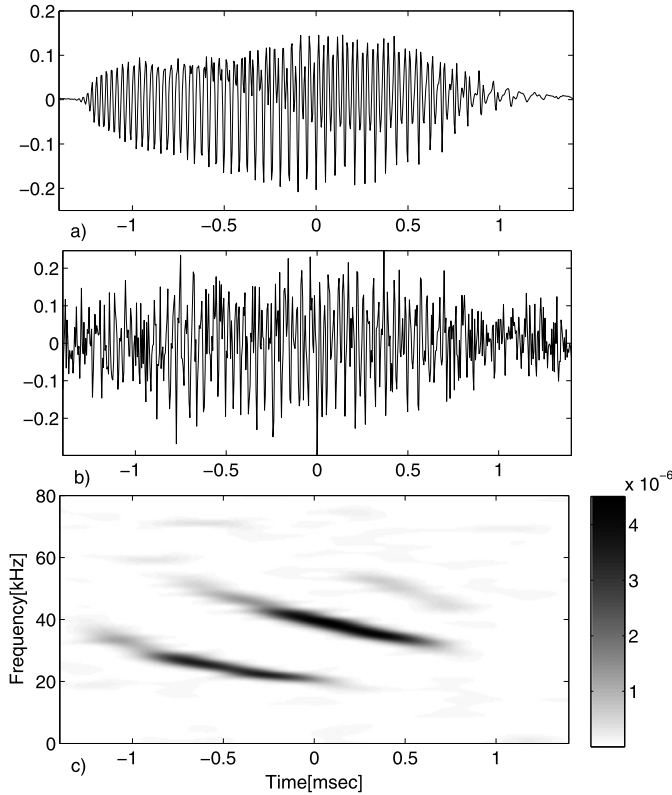| Norm. App. Err/Comp.	$p_1(t)$	$p_2(t)$	$p_3(t)$
e^{cv}	−14.7	−16.1	−14.3
e^w	−14.3	−15.6	−14.8
ed	0.17	0.25	0.21

Fig. 20. (a) Echolocation pulse emitted by the Large Brown Bat, Eptescius Fuscus; (b) its noisy version at 0 dB; (c) spectrogram of the noisy signal. While computing the spectrogram in (b), a Gaussian window with standard deviation $\sigma = 14 \times 10^{-5}$ s was used.

Fig. 21. (a) Sum of the estimated components and (b) its spectrogram. While computing the spectrogram, a Gaussian window with standard deviation $\sigma = 14 \times 10^{-5}$ s was used. (c) Obtained both auto-cross-term and cross–cross-term free Wigner–Ville distributions of the echolocation pulse.

the three components $p_1(t)$, $p_2(t)$, $p_3(t)$ in this signal, proposed method is utilized by using both Chan–Vese and Watershed segmentation [37] techniques. For each component two different estimates are obtained $\tilde{p}_k^{cv}(t)$, $\tilde{p}_k^w(t)$, $k = 1, 2, 3$, where the superscript cv and w denote the estimates based on Chan–Vese and Watershed segmentation techniques, respectively. The corresponding normalized approximation errors $e_k^{cv} = 10 \log(\frac{\|p_k(t)-\tilde{p}_k^{cv}(t)\|^2}{\|p_k(t)\|^2})$, $e_k^w = 10 \log(\frac{\|p_k(t)-\tilde{p}_k^{w}(t)\|^2}{\|p_k(t)\|^2})$ and normalized energy difference percentages $ed_k = 100 \frac{\|\tilde{p}_k^{cv}(t)-\tilde{p}_k^{w}(t)\|^2}{\|\tilde{p}_k^{cv}(t)\|^2}$ are tabulated in Table 2. As observed, there is no significant difference between the signal components estimate by utilizing two different segmentation techniques.

Finally, we tested our method on two real signals. The first one is the bat echolocation signal [38] shown in Fig. 20(a). It is a 2.8 ms echolocation pulse emitted by the Large Brown Bat, Eptescius Fuscus. We added synthetically generated circularly symmetric white noise such that the SNR was set to 0 dB. The resulting noise corrupted signal and its spectrogram are shown in Fig. 20(b) and (c), respectively. By applying the proposed multi-component analysis technique, the strongest 3 components have been identified and extracted. The approximation orders were estimated to be 4 for the first (occurring at time 0.5 ms and 50 kHz), 9 for
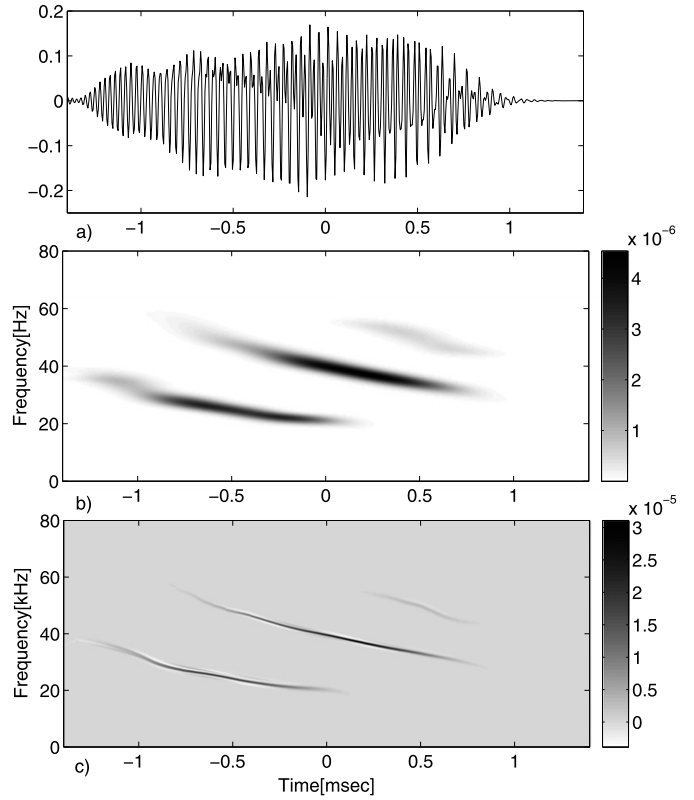
the second (occurring at time 0.1 ms and 40 kHz) and 8 for the third component (occurring at time −0.5 ms and 25 kHz), using (48). The sum of estimated components is plotted in Fig. 21(a). The normalized approximation error between this signal and the original one shown in Fig. 20(a) is around −11.7 dB. This error was around −14.8 dB when we analyzed the original noise-free signal. Its spectrogram is given in Fig. 21(b). Comparing this plot with Fig. 20(c), proposed multi-component analysis method estimated the signal components reliably.

To obtain a high resolution time–frequency representation of this multi-component signal, we used Wigner–Ville distribution (WVD). WVD provides the highest time–frequency resolution for a mono-component signal which has linear frequency modulation. However, direct computing WVD of a multi-component signal generates alien energy localizations, which do not actually exist in the signal, in the resulting time–frequency representation. These alien energy localizations are referred as cross-terms or cross–cross-terms. To eliminate cross-terms, WVD of each component estimated by the proposed method is computed and superposed. However, since none of the estimated components has exact linear instantaneous frequency, WVD of each component still has alien energy localizations. This time, these alien energy localizations are referred as auto-cross terms. Auto-cross terms can also be eliminated by the proposed method. When the pre-processing stage is applied to the signal component, the resulting signal has its component under analysis with a compact circular support without significant non-linear frequency variation. Once HG representation is applied on to the signal extracting the component under analysis, the obtained signal doesn't generate auto-cross terms in its WVD. Then, inverse transforms (post-processing stage) is applied to the computed WVD. Let $\tilde{s}_s^k(t)$, $k = 1, 2, 3$ denote the estimate of the kth component after the pre-processing stage given in (34) and
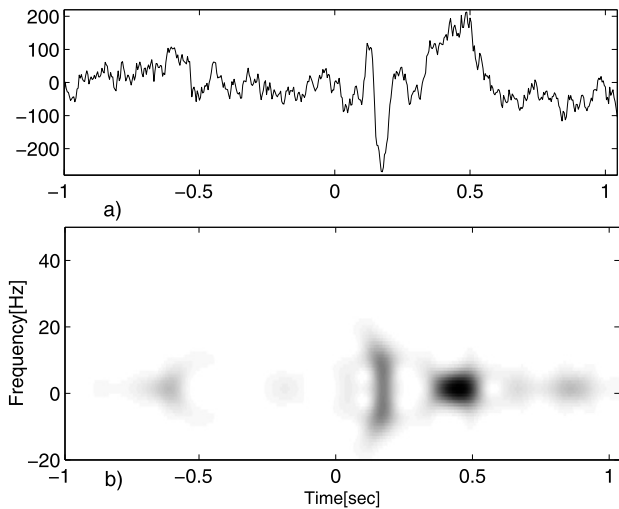
Fig. 22. (a) EEG recording and (b) its spectrogram. While computing the spectrogram, a Gaussian window with standard deviation $\sigma = 0.1/\sqrt{2\pi}$ s was used.
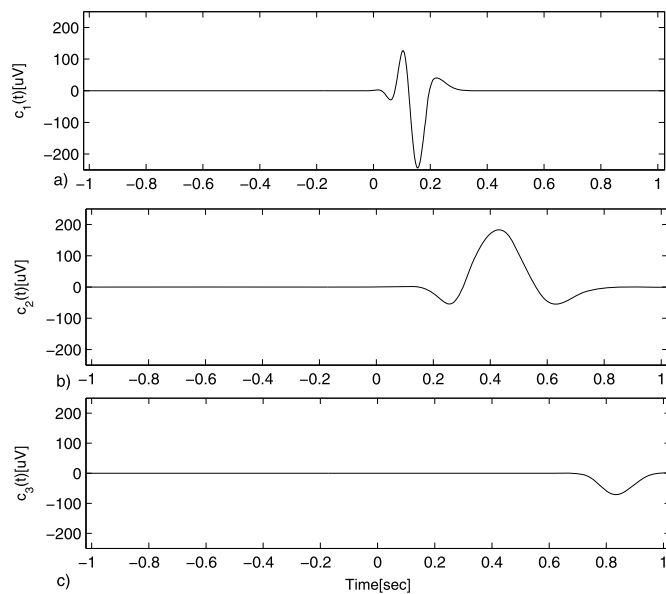

Fig. 23. Estimated signal components (a)–(c) from the EEG recording shown in Fig. 22.

$WV_s^k(t, f)$ denote its WVD. The auto-cross-term-free WVD of $\tilde{s}_k(t)$ is given by:

$$WV^k(t, f) = \frac{1}{v^k} WV_s^k\left(\frac{t - t_c^k}{v^k}, v^k\left(f - f^k(t)\right)\right), \qquad (56)$$

where $\{t_c^k, f^k(t), v^k\}$, $k = 1, 2, 3$ are the transform parameters. The sum $WV(t, f) = WV^1(t, f) + WV^2(t, f) + WV^3(t, f)$ is both auto-cross term and cross–cross-term free WVD of the bath echolocation pulse and shown in Fig. 21(c).

The second real signal that we analyzed is a 2 s EEG recording (1 sec pre, 1 sec post stimulus), stimulated by an oddball paradigm shown in Fig. 22 [39]. Only the post stimulus region (time > 0 s) was analyzed. 3 components were identified and extracted by the proposed method. Estimated components $c_1(t)$, $c_2(t)$, $c_3(t)$ are shown in Figs. 23(a), (b), (c), respectively. In Fig. 24(a), the original recording $x(t)$ (solid-black) and sum of the estimated components $\tilde{c}(t) = c_1(t) + c_2(t) + c_3(t)$ are plotted. To provide comparisons, wavelet based denoising method in [39] has also been implemented and applied to the recording only for the post stimu-
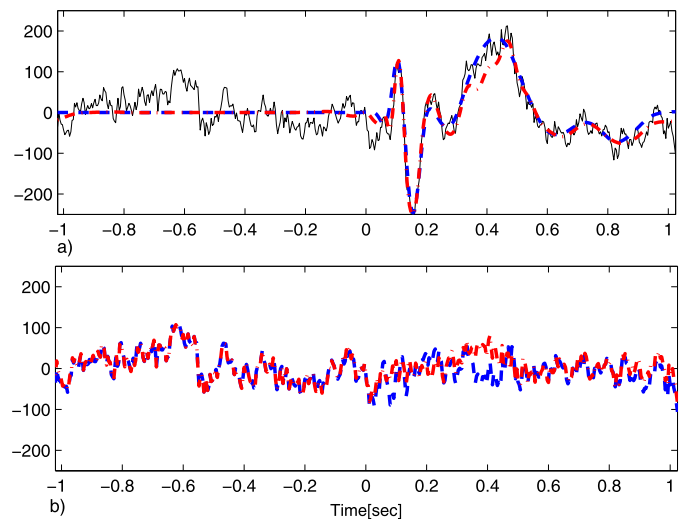

Fig. 24. (a) Original EEG recording (solid-black), sum of the estimated components (dashed-blue), wavelet denoising result (dotted-dashed-red). (b) Residuals for the proposed method (dashed-blue) and wavelet denoising (dotted-dashed-red). (For interpretation of the references to color in this figure legend, the reader is referred to the web version of this article.)

lus interval. The resulting denoised signal $\hat{c}(t)$ (dashed-dotted-red) is given in Fig. 24(a). In Fig. 24(b), the residuals $\tilde{r}(t) = x(t) - \hat{x}(t)$ (dashed-blue) and $\hat{r}(t) = x(t) - \hat{c}(t)$ are also shown. As observed, superposition of the estimated components by our method provides a better fit to the original recording. Note that, while the wavelet method returns only the total denoised signal, our method is capable of providing each individual signal component buried in the available observation.

6. Conclusions

A new fully automated signal analysis technique is proposed for decomposition of signals into its components that have compact TFSs. The proposed approach utilizes HG functions that are adapted to the identified TFSs of the individual signal components. To fully achieve the optimal localization properties of the HG function expansion, a pre-processing technique is developed to transform the support of a chosen signal component to a circular one centered around the origin. Also an EM like iterative procedure is developed for accurate analysis of multi-component signals. Robust techniques are introduced for reliable estimation of pre-processing and expansion parameters. Obtained results show that proposed method provides reliable identification and extraction of signal components even under severe noise cases.

References

[1] J.B. Martens, The Hermite transform: a survey, EURASIP J. Appl. Signal Process. 2006 (2006) 1–20.
[2] W. Park, G. Leibon, D.N. Rockmore, G.S. Chirikjian, Accurate image rotation using Hermite expansions, IEEE Trans. Image Process. 18 (2009) 1988–2003.
[3] S. Stanković, I. Orović, A. Krylov, Video frames reconstruction based on time–frequency analysis and Hermite projection method, EURASIP J. Adv. Signal Process. 2010 (2010) 1–11.
[4] J. Silva, M. Campos, Spectrally efficient UWB pulse shaping with application in orthogonal PSM, IEEE Trans. Commun. 55 (2007) 313–322.
[5] A. Mahadevan, S. Acharya, D.B. Sheffer, D.H. Mugler, Ballistocardiogram artifact removal in EEG-fMRI signals using discrete Hermite transforms, IEEE J. Sel. Top. Signal Process. 2 (2008) 839–853.
[6] W. Jiang, S.G. Kong, Block-based neural networks for personalized ECG signal classification, IEEE Trans. Neural Netw. 18 (2007) 1750–1761.
[7] I. Orović, S. Stanković, T. Chau, C.M. Steele, E. Sejdić, Time–frequency analysis and Hermite projection method applied to swallowing accelerometry signals, EURASIP J. Adv. Signal Process. 2010 (2010) 1–7.

[8] M.M. Rao, T.K. Sarkar, T. Anjali, R.S. Adve, Simultaneous extrapolation in time and frequency domains using Hermite expansions, IEEE Trans. Antennas Propag. 47 (1999) 1108–1115.

[9] P.L. Carro, J.D. Mingo, Ultrawide-band antenna distortion characterization using Hermite–Gauss signal subspaces, IEEE Antennas Wirel. Propag. Lett. 7 (2008) 267–270.

[10] I. Orović, S. Stanković, T. Thayaparan, L. Stanković, Multiwindow s-method for instantaneous frequency estimation and its application in radar signal analysis, IET Signal Process. 4 (2010) 363–370.

[11] J. Xiao, P. Flandrin, Multitaper time–frequency reassignment for nonstationary spectrum estimation and chirp enhancement, IEEE Trans. Signal Process. 55 (2007) 2851–2860.

[12] M. Bayram, R.G. Baraniuk, Multiple Window Time-Varying Spectrum Estimation in Nonlinear and Nonstationary Signal Processing, Cambrigde Univ. Press, Cambridge, 2000.

[13] F. Cakrak, P.J. Loughlin, Multiple window time-varying spectral analysis, IEEE Trans. Signal Process. 49 (2001) 448–453.

[14] V.C. Chen, H. Ling, Joint time–frequency analysis for radar signal and image processing, IEEE Signal Process. Mag. 16 (1999) 81–93.

[15] M. Ning, D. Vray, Bottom backscattering coefficient estimation from wideband chirp sonar echoes by chirp adapted time–frequency representation, in: Proceedings of the 1998 IEEE International Conference on Acoustics, Speech and Signal Processing, Seattle, USA, pp. 2461–2464.

[16] R.G. Baraniuk, M. Coates, P. Steeghs, Hybrid linear/quadratic time–frequency attributes, IEEE Trans. Signal Process. 49 (2001) 760–766.

[17] B. Boashash, P. O'shea, Time–frequency analysis applied to signaturing of underwater acoustic signals, in: Proceedings of the 1988 IEEE International Conference on Acoustics, Speech and Signal Processing, New York, USA, pp. 2817–2820.

[18] O. Yilmaz, S. Rickard, Blind separation of speech mixtures via time–frequency masking, IEEE Trans. Signal Process. 52 (2004) 1830–1847.

[19] A.K. Ozdemir, S. Karakas, E.D. Cakmak, D.I. Tufekci, O. Arikan, Time–frequency component analyser and its application to brain oscillatory activity, J. Neurosci. Methods 145 (2005) 107–125.

[20] A.K. Ozdemir, Time–frequency component analyzer, Ph.D. thesis, Bilkent University, Ankara, Turkey, 2003.

[21] L. Durak, O. Arikan, Short-time Fourier transform: two fundamental properties and an optimal implementation, IEEE Trans. Signal Process. 51 (2003) 1231–1242.

[22] I. Daubechies, The wavelet transform, time–frequency localization and signal analysis, IEEE Trans. Inform. Theory 36 (1990) 961–1005.

[23] S. Mann, S. Haykin, The chirplet transform: physical considerations, IEEE Trans. Signal Process. 43 (1995) 2745–2761.

[24] N. Nebedev, Special Functions and Their Applications, Dover, New York, 1972.

[25] P. Flandrin, Maximum signal energy concentration in a time–frequency domain, in: Proceedings of the 1988 IEEE International Conference on Acoustics, Speech and Signal Processing, New York, USA, pp. 2176–2179.

[26] I. Daubechies, Time–frequency localization operators: a geometric phase space approach, IEEE Trans. Inform. Theory 34 (1988) 605–612.

[27] F. Hlawatsch, Time–Frequency Analysis and Synthesis of Linear Signal Spaces, Kluwer, 1998.

[28] L.R. Conte, R. Merletti, G.V. Sandri, Hermite expansions of compact support waveforms: applications to myelectric signals, IEEE Trans. Biomed. Eng. 41 (1994) 1147–1159.

[29] M. Abramowitz, I. Stegun, Handbook of Mathematical Functions, Dover, New York, 1965.

[30] G. Cincotti, F. Gori, M. Santarsiero, Generalized self Fourier functions, J. Phys., A, Math. Gen. 25 (1992) 1191–1194.

[31] H. Ozaktas, B. Barshan, D. Mendlovic, L. Onural, Convolution, filtering and multiplexing in fractional Fourier domains and relations to chirp and wavelet transforms, J. Opt. Soc. Amer. A 11 (1994) 547–559.

[32] L. Cohen, Time–Frequency Analysis, Prentice Hall PTR, Englewood Cliffs, NJ, 1995.

[33] T.F. Chan, L.A. Vese, Active contours without edges, IEEE Trans. Image Process. 10 (2001) 266–277.

[34] D.L. Donoho, De-noising by soft thresholding, IEEE Trans. Inform. Theory 41 (1995) 613–627.

[35] I. Daubechies, Ten Lectures on Wavelets, SIAM, 1992.

[36] D.L. Donoho, M. Johnstone, Adapting to unknown smoothness via wavelet shrinkage, J. Amer. Statist. Assoc. 90 (1995) 1200–1224.

[37] J.K.L. Shafarenko, M. Petrou, Automatic watershed segmentation of randomly textured color images, IEEE Trans. Image Process. 6 (1997) 1530–1544.

[38] Bat echolocation signal, http://dsp.rice.edu/software/bat-echolocation-chirp, 2009.

[39] R. Quiroga, Obtaining single stimulus evoked potentials with wavelet denoising, Physica D 145 (2000) 278–292.

Yaşar Kemal Alp was born in Konya, Turkey, in 1985. He received his B.Sc. degree in electrical and electronics engineering from Bilkent University, Ankara, Turkey. He worked as a Research Scientist in Schlumberger Cambridge Research between June–August 2009 and July–September 2010. He is currently pursuing his Ph.D. in Department of Electrical and Electronics Engineering, Bilkent University. His research interests are time–frequency signals analysis, inverse problems and their applications to radar signal processing.

Orhan Arıkan was born in 1964 in Manisa, Turkey. He received the B.Sc. degree in electrical and electronics engineering from the Middle East Technical University, Ankara, Turkey in 1986 and both the M.S. and Ph.D. degrees in electrical and computer engineering from the University of Illinois, Urbana-Champaign, in 1988 and 1990, respectively. Following his graduate studies, he worked for three years as a Research Scientist at Schlumberger – Doll Research, Ridgefield, CT. He joined Bilkent University in 1993, where he is presently Professor of Electrical Engineering since 2006 and chair of the Electrical Engineering Department since 2011. His current research interests are in statistical signal processing, time–frequency analysis, and array signal processing.